Arkansas Tech University

Online Research Commons @ ATU

Faculty Publications - Physical Sciences

Department of Physical Sciences

4-1-2011

The Chromospheric Activity of [HH97 FS Aur-79: a Close Binary With Late-Type Active (Dk7E+Dm3E) Components

S. J. Austin

Jeff W. Robertson
Arkansas Tech University

T. R. De Souza

C. Tycner

R. K. Honeycutt

Follow this and additional works at: https://orc.library.atu.edu/faculty_pub_phys

Part of the Physical Sciences and Mathematics Commons

THE CHROMOSPHERIC ACTIVITY OF [HH97] FS Aur-79: A CLOSE BINARY WITH LATE-TYPE ACTIVE (dK7e+dM3e) COMPONENTS

S. J. AUSTIN[1], J. W. ROBERTSON[2], T. R. DE SOUZA[3], C. TYCNER[4], AND R. K. HONEYCUTT[5]

[1] Department of Physics and Astronomy, University of Central Arkansas, Conway, AR 72035, USA; saustin@uca.edu
[2] Department of Physical Sciences, Arkansas Tech University, Russellville, AR 72801-2222, USA; jrobertson@atu.edu
[3] Departamento de Física, GAS, Universidade Federal de Santa Catarina, Grupo de Astrofísica da UFSC,
Campus Trinidade, 88040-900 Florianópolis, SC, Brazil; tiago@astro.ufsc.br
[4] Department of Physics, Central Michigan University, Mount Pleasant, MI 48859, USA; c.tycner@cmich.edu
[5] Department of Astronomy, Indiana University, Bloomington, IN 47405, USA; honey@astro.indiana.edu

ABSTRACT

Using Doppler tomography we show that FS Aur-79, a near-contact close binary system with late-type active dK7e+dM3e components, has chromospheric prominences in two distinct emission regions associated with the primary star and a larger amount of chromospheric activity associated with the cooler secondary star. The line profiles, equivalent widths, and equivalent width ratios of the Hα and Hβ emission lines as a function of orbital phase further support that the majority of the chromospheric emission originates above the secondary star and near the neck region. Analysis of high-resolution spectra using the technique of broadening functions has enabled us to determine the radial velocity of the secondary star near quadratures to be approximately 224 km s^{-1}. A Wilson–Devinney model of the system fitting the *UBV* light curves and radial velocities shows that there are star spots near the chromospherically active regions. Finally, the absence of Li I λ6708 in the spectra lets us put a lower limit on the age of this system to at least 500 Myr.

Key words: binaries: close – binaries: eclipsing – binaries: spectroscopic – stars: late-type

Online-only material: color figures

1. INTRODUCTION

Good, accurate, fundamental parameters for late-type main-sequence stars are based on only a handful of double-lined spectroscopic, eclipsing binaries with K and M components. FS Aur-79 (Henden & Honeycutt 1997; Robertson et al. 2004; Austin et al. 2007) is a short-period (0.2508 days) close eclipsing binary with chromospherically active K and M components. Very few systems in the lists of near-contact binaries (Shaw 1990; Shaw et al. 1996) have spectral types later than F and none have spectral types of M, making this system quite rare. A handful of stars that are the closest siblings to this system include YY Gem and CM Dra (Strassmeier et al. 1988; Chabrier & Baraffe 1995; Morales et al. 2009), CU Cnc (Ribas 2003), BW3 V38 (Macaroni & Montalban 2004), and RE 0618+75 (Jeffries et al. 1993) along with their contact cousins, W Cor (Odell 1996), VZ Psc (Hrivnak et al. 1995), for example, and those listed by Hilditch et al. (1988), although none of those contact systems have a dMe component. Near-contact and contact systems with these very late components are extremely rare and are therefore interesting for what they can tell us about binary stellar formation and evolution.

In Austin et al. (2007), we analyzed high signal-to-noise multi-color light curves and found this to be a near-contact binary system with two star spots on the primary and one star spot on the secondary. The following system parameters were also determined: a primary star of mass $0.59 \pm 0.02\ M_\odot$, temperature 4100 ± 25 K, mean radius of $0.67\ R_\odot$, just filling its Roche lobe and a secondary star of mass $0.31 \pm 0.09\ M_\odot$, temperature 3425 ± 25 K, mean radius of $0.48\ R_\odot$, just within its Roche lobe. An inclination angle of $83^\circ \pm 2^\circ$ with a center of mass separation of $1.62\ R_\odot$ was also derived. The low-resolution spectrum analyzed in Austin et al. (2007) was consistent with the primary and secondary components having spectral types

of dK7e and dM3e, respectively. The high-resolution spectra analyzed in Austin et al. (2007) appeared upon visual inspection to be single-lined and thus provided only a radial velocity curve for the primary star. Both the high- and low-resolution spectra analyzed in Austin et al. (2007) showed Hα and Hβ in emission confirming chromospheric activity and possibly the presence of circumstellar material.

To better understand the chromospheric activity of FS Aur-79, we have analyzed the equivalent widths with phase for the Hα and Hβ emission and produced a Doppler tomogram for the system from the Hα emission. Using broadening functions (Rucinski 1999), we have deconvolved the primary and secondary star contributions to the line profiles and found the radial velocity of the secondary near phases 0.25 and 0.75. We have verified the binary star model with star spots utilizing the Wilson–Devinney modeling code (Wilson & Devinney 1971) simultaneously fitting the photometry and radial velocities. In Section 2, we describe how the photometry and spectroscopy were obtained and reduced. In Section 3, we present our broadening function (BF), equivalent width, Doppler tomography (DT), and binary modeling analyses. Section 4 presents the final discussion and summary of our conclusions.

2. OBSERVATIONS AND REDUCTIONS

In Austin et al. (2007), we described how we obtained and reduced the photometric and spectroscopic data. Here, we repeat the description for the data used specifically in this study.

2.1. HET HRS Spectroscopy

We obtained 10 hr of priority-2 time during 2005 semester B (September through January) on the High Resolution Spectrograph (HRS) at the 9.2 m Hobby–Eberly Telescope (HET) through NOAO. Due to the nature of the HET service
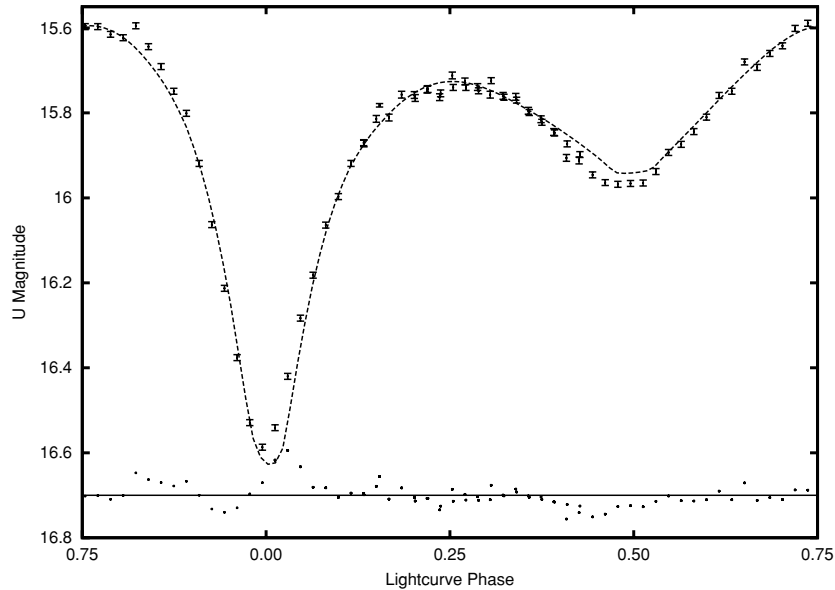
Figure 1. Phased *U*-band photometry from Austin et al. (2007) shown with error bars. Dashed curve is the resulting *U*-band light curve from the best-fit Wilson–Devinney model. Dots are the observed minus computed residuals where the solid horizontal line at a magnitude of 16.7 represents the zero residual level.

observing scheduling only one object spectrum per half-night was possible. In order to get as complete a sampling over an orbit as possible, we requested that observations be done as randomly in time as possible over the semester, avoiding consecutive nights at the same time of night due to the approximately 6 hr period of the orbit. The HRS configuration yielding a resolving power of 15,000, wavelength coverage of approximately 4076–7838 Å, a fiber with an angular diameter on the sky of 3″, one sky fiber, no image slicer, no iodine gas cell, and binning of 2 × 5 for 3.2 pixels per resolving elements were used. Bias, flat, and Th–Ar comparison lamp frames were also obtained by the night observers for reduction and calibration purposes. Spectral standards were also obtained, giving us the option to relative flux calibrate the spectra.

Standard IRAF tasks were used to process the frames into one-dimensional spectra normalized to the continuum. The following reduction steps were used for both the red and blue channels: `zerocombine`, `flatcombine`, `ccdproc` to trim and apply the zero correction, `cosmicrays`, `apall` used to find and define the apertures for each spectral order on the red and blue chips, `apscatter` to remove any scattered light, `apflatten` to get a flat-field solution using the combined flat, and `ccdproc` to apply the flattening to the spectral frames, `apall` once again to extract the spectral orders. HET HRS orders 78–145 were extracted corresponding to spectral coverage from 4200 Å to 7900 Å. When necessary, sky substraction was done for those nights near full moon when the sky background was significant and for those orders which have problematic sky lines (i.e., order 104, Na I-D doublet). Wavelength calibration was done for each spectral order of interest using `ident`, `reident`, `refspec`, and `dispcor`. The spectra were then converted to the heliocentric frame of reference using `rvcor` and `dopcor`. The instrumental flux was then normalized to the continuum by using either `contin` if it could correctly find the continuum, or by doing the continuum fitting interactively using the option under `splot`.

2.2. USNO Photometry

Photometric observations obtained at the U.S. Naval Observatory (USNO), Flagstaff Station, were acquired using the 1 m Ritchey–Chrétien telescope. The telescope was equipped with a Tektronix 2048 × 2048 thinned back-illuminated CCD and Johnson *UBV* filters. The camera has a scale of 0.68 arcsec pixel^{-1}, which results in a field of view of 23.2 by 23.2 arcmin.

The field centered on FS Aur-79 was observed on three consecutive nights, 2005 December 4, 5, and 6 (UT), in *B*, *V*, and *U* filters, respectively. Each set of nightly observations was preceded with a set of 20–50 bias frames and 10 dome flats in all three filters. A total of 110, 176, and 73 individual exposures were obtained in the *B*, *V*, and *U* filters, respectively. Each night the field was observed during an 8 hr window, which corresponded to hour angles between −4 and +4 hr. Although each night was devoted to a single filter, at least one set of exposures in all three filters was also acquired each night. The typical seeing during the USNO observing run was between 2 and 3 arcsec.

All of the CCD images containing photometry data were processed using `Cmuniwin`.[6] This PC-based software with a graphical user interface was converted from Linux C programs originally developed by Hroch (1998). In short, the images are (1) converted to FITS if necessary; (2) flat-fielded and dark-subtracted if desired; (3) processed to find stellar targets and photometrically measured utilizing the algorithms of DAOPHOT (Stetson 1987); (4) target lists are pattern-matched to identify stars in each image via the algorithm of Groth (1986); and (5) variable, comparison, and check stars are selected to generate differential photometry and light curves.

The comparison and check stars used for the differential photometry were the secondary standard stars FS Aur-62 and FS Aur-63 (Henden & Honeycutt 1997). The *U*, *B*, and *V* magnitudes of FS Aur-79 were converted to standard magnitudes (shown in Figures 1–3) using the *U*, *B*, and *V* magnitudes of the standard star FS Aur-62 (*U* = 13.795 ± 0.005, *V* = 13.650 ± 0.004, *B* − *V* = 0.412 ± 0.003; Henden & Honeycutt 1997; A. A. Henden 2006, private communication).

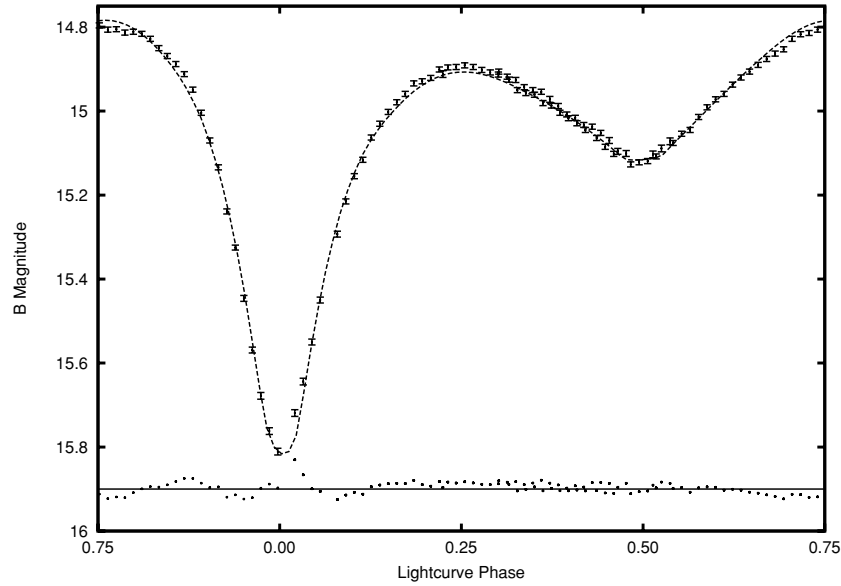[6] http://c-munipack.sourceforge.net

Figure 2. Phased *B*-band photometry from Austin et al. (2007) shown with error bars. Dashed curve is the resulting *B*-band light curve from the best-fit Wilson–Devinney model. Dots are the observed minus computed residuals where the solid horizontal line at a magnitude of 15.9 represents the zero residual level.
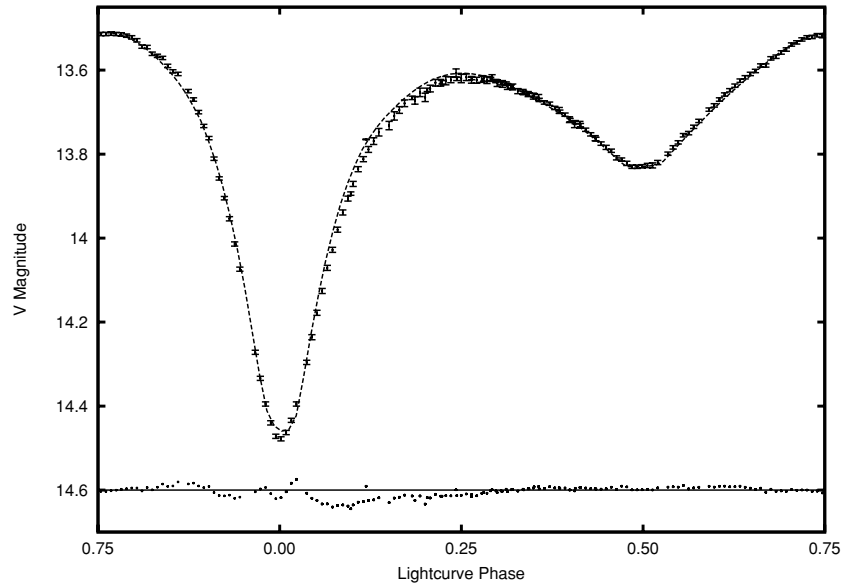

Figure 3. Phased *V*-band photometry from Austin et al. (2007) shown with error bars. Dashed curve is the resulting *V*-band light curve from the best-fit Wilson–Devinney model. Dots are the observed minus computed residuals where the solid horizontal line at a magnitude of 14.6 represents the zero residual level.

3. ANALYSIS

3.1. Spectral Broadening Functions

In Figure 4, we show the trailed and interpolated spectrum of the Hα emission line along with the expected motion of the primary and secondary stars. From this representation it is difficult to follow the orbital motion of the two stars but it is possible to see that the line is composed of two anti-phased components of different velocities partially following the expected motion of the two stars. The cross-correlation method used in Austin et al. (2007) was unsuccessful in detecting the secondary star. We employed the spectral BF technique as described by Rucinski (1999) using the Windows interface prepared by Bob Nelson (Broad15.exe[7]) following the

procedures described in Rucinski's cookbook.[8] We used the best signal-to-noise (S/N) spectral orders near orbital phase 0.5 as the templates and applied BF to the spectral orders 94, 95, 100, 104, 109, 112, 116, 118, and 123 shown in Figures 5–13. Phase 0.5 was chosen for the template, since this represents a view of this system that is one star (the primary) at zero radial velocity. Figure 14 shows an example of one of the BFs generated by the BF technique. Averaging the results for orders listed above for the orbital phases with high enough Doppler shifting (near phases 0.25 and 0.75) are shown in Figure 15. Figure 15 shows the BF radial velocities for the primary and secondary stars, the radial velocities of the primary measured from Austin et al. (2007), and the modeled radial velocity curves from the binary star model that we describe later in this paper. The radial velocity of the primary star determined using the BF method is consistent
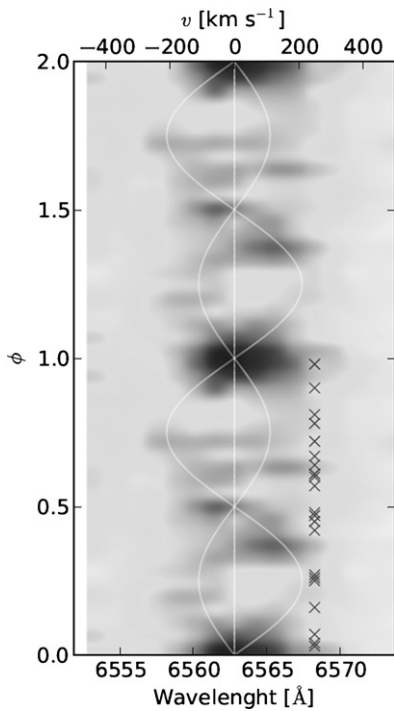
---

[7] http://members.shaw.ca/bob.nelson/software1.htm

[8] http://www.astro.utoronto.ca/~rucinski/SVDcookbook.html

Figure 4. Trailed spectra for the Hα emission line and repeated in phase. White solid curves are the radial velocities of the primary and secondary stars while the vertical line represents the rest wavelength in the frame of the binary. The horizontal crosses represent the phases in which the data were acquired.

with the radial velocity measured from the Doppler shifting of the lines from Austin et al. (2007). The radial velocities of the secondary star found by the BF method are also consistent with those inferred from our light curve modeling solutions. The average velocities of the stars from the BF method near the quadratures were $v_1 = 121 \pm 12$ km s^{-1} and $v_2 = 224 \pm 4$ km s^{-1}. For an inclination $i \approx 90°$, the mass ratio from these velocities gave us $q = 0.540 \pm 0.053$, which is consistent with the photometrically determined ratio from light curve modeling of $q = 0.527 \pm 0.030$ found in Austin et al. (2007). Also, given the period and $i \approx 90°$ the semi-major axis of the system should be $a = 1.75 \pm 0.08$ $R_\odot$, the system mass $M_{\text{total}} = 1.12 \pm 0.16$ $M_\odot$, the mass of the primary $M_1 = 0.73 \pm 0.25$ $M_\odot$, and the mass of the secondary $M_2 = 0.39 \pm 0.08$ $M_\odot$. The values of a, M_{total}, M_1, and M_2 are all a bit larger than those found in Austin et al. (2007), but are within and/or have overlapping error bars.

3.2. Hα and Hβ Line Profiles and Equivalent Widths

Hα and Hβ in emission are indicators of chromospheric activity. Figures 16 and 17 show examples of the emission line profiles of Hα and Hβ at various phases. The line profiles have a more single-peak appearance around 0.0 and 0.5 phases, and more of a double-peak profile near 0.25 and 0.75.

Figure 18 shows the equivalent widths of the chromospheric emission of Hα and Hβ. The equivalent widths of the profiles were measured with the equivalent width function in the IRAF task *splot*. For phases where the line was difficult to detect, the wavelength range integrated was the same as that used for the
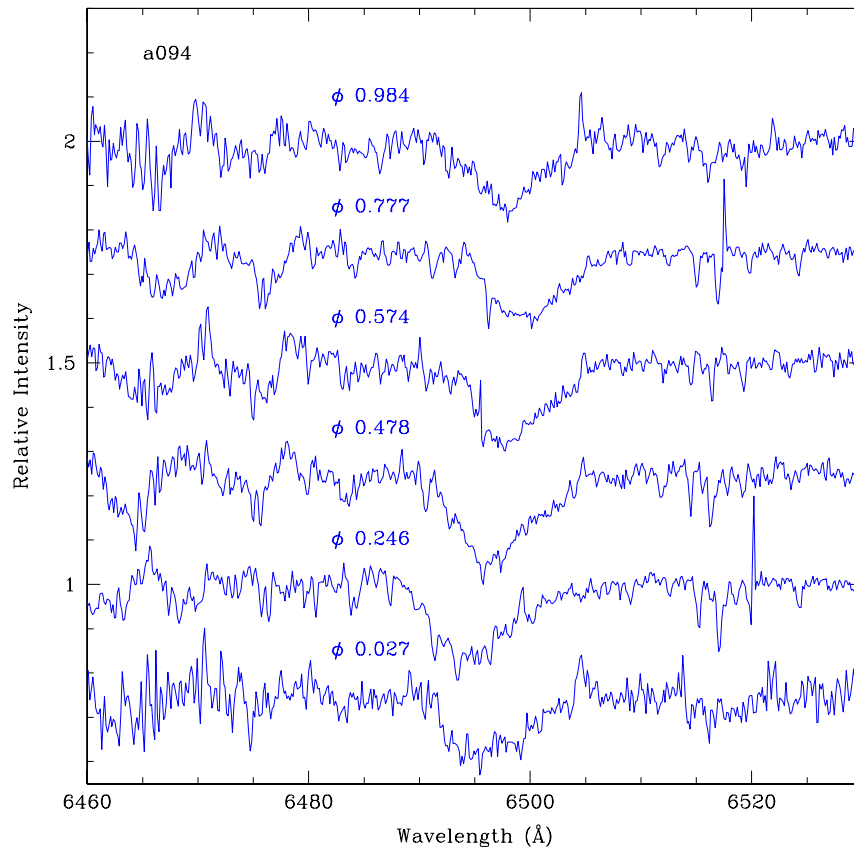

Figure 5. Spectra of the Fe I λ6494.9, λ6498.9 Ba II λ6496.8, Ca I λ6493.7, λ6499.6 blend at various orbital phases (φ). The spectra are from HET HRS order 94 and with the flux normalized to the continuum.

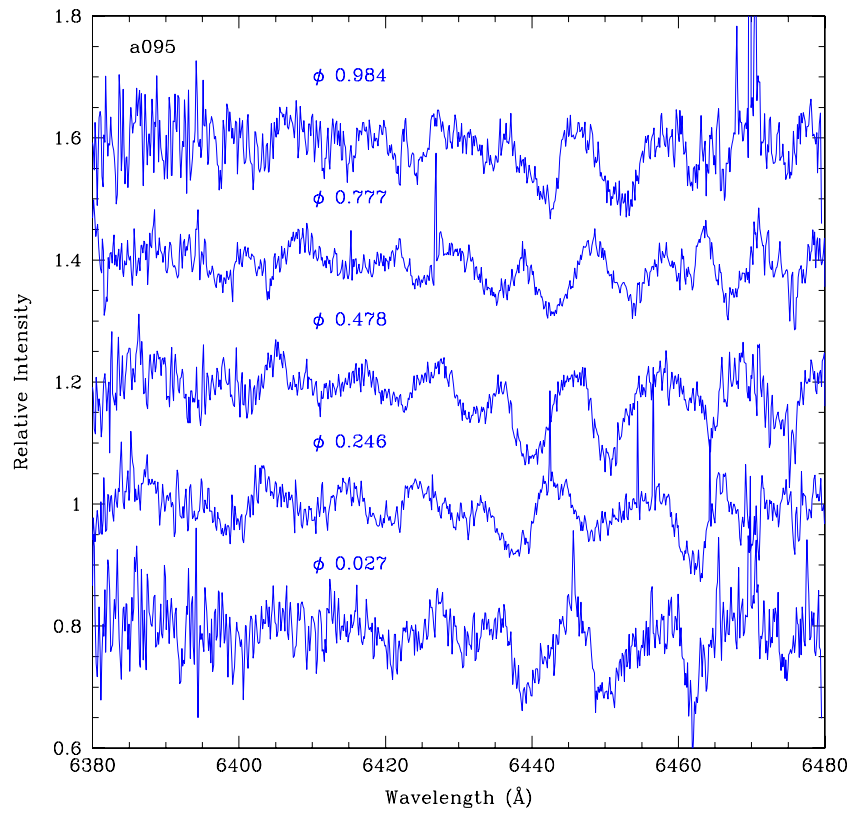(A color version of this figure is available in the online journal.)

Figure 6. Spectra of lines Fe I λ6399.6, 6400, λ6419.9 6421.3, λ 6430.8 6462.7 Ca I λ6399.7, λ6439.0, λ6449, λ6462.5 at various orbital phases (φ). The spectra are from HET HRS order 95 and with the flux normalized to the continuum.

(A color version of this figure is available in the online journal.)

Figure 7. Spectra of lines Ca I λ6103, λ6122, Fe I λ6136.6, λ6136.9, λ6137.7 at various orbital phases (φ). The spectra are from HET HRS order 95 and with the flux normalized to the continuum.

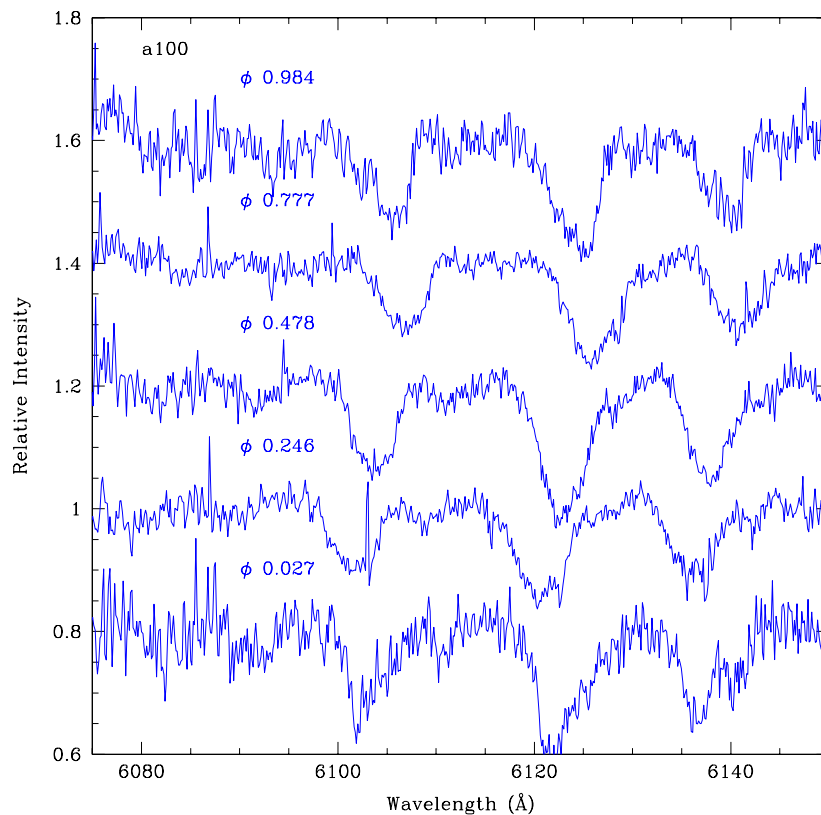(A color version of this figure is available in the online journal.)

Figure 8. Spectra of lines Ca I λ5857.4 Fe I λ5859.5, λ5862.3, Na I λ5893 at various orbital phases (φ). The spectra are from HET HRS order 95 and with the flux normalized to the continuum.

(A color version of this figure is available in the online journal.)
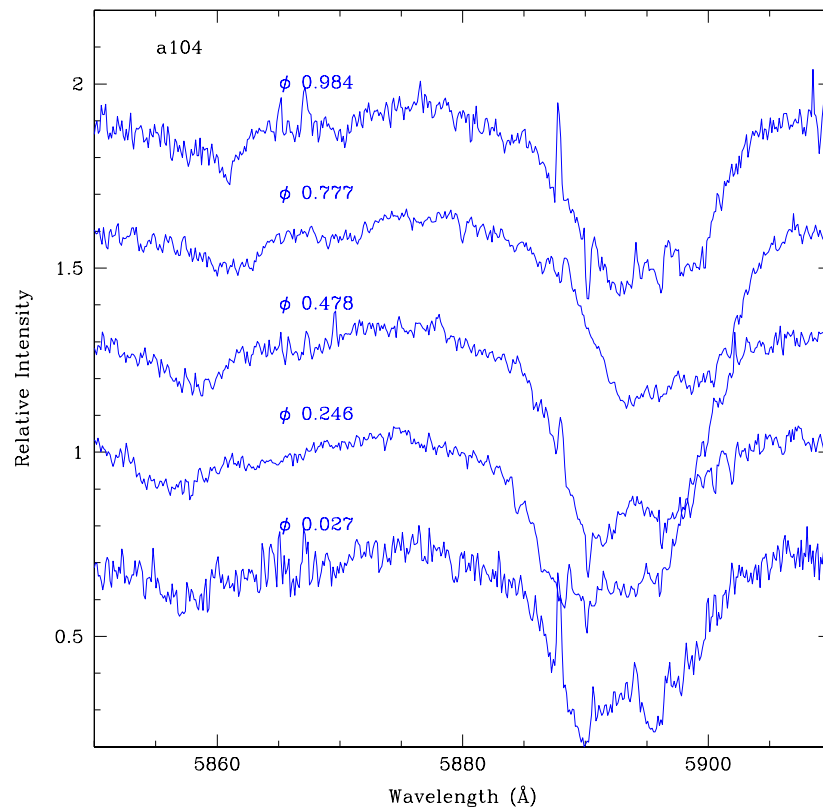

Figure 9. Spectra of lines Ca I λ5602.8, Fe I λ5602.9, λ5615.3, λ5615.6, λ5624.5 at various orbital phases (φ). The spectra are from HET HRS order 95 and with the flux normalized to the continuum.

(A color version of this figure is available in the online journal.)

Figure 10. Spectra of lines Fe I λ5446.8, λ5455.5, λ5462.9, λ5463.3 at various orbital phases (ϕ). The spectra are from HET HRS order 95 and with the flux normalized to the continuum.

(A color version of this figure is available in the online journal.)
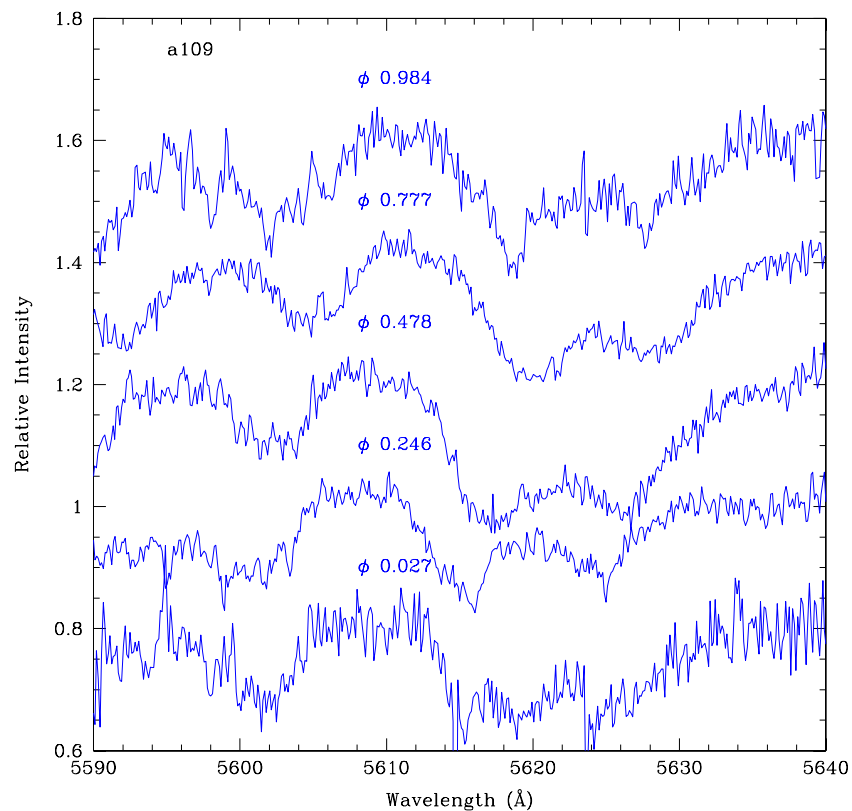

Figure 11. Spectra of lines Fe I λ5269.5, λ5270.35, λ5281.7, λ5283.6, λ5300.8, λ5302.3, Ca I λ5270.2 at various orbital phases (ϕ). The spectra are from HET HRS order 95 and with the flux normalized to the continuum.

(A color version of this figure is available in the online journal.)
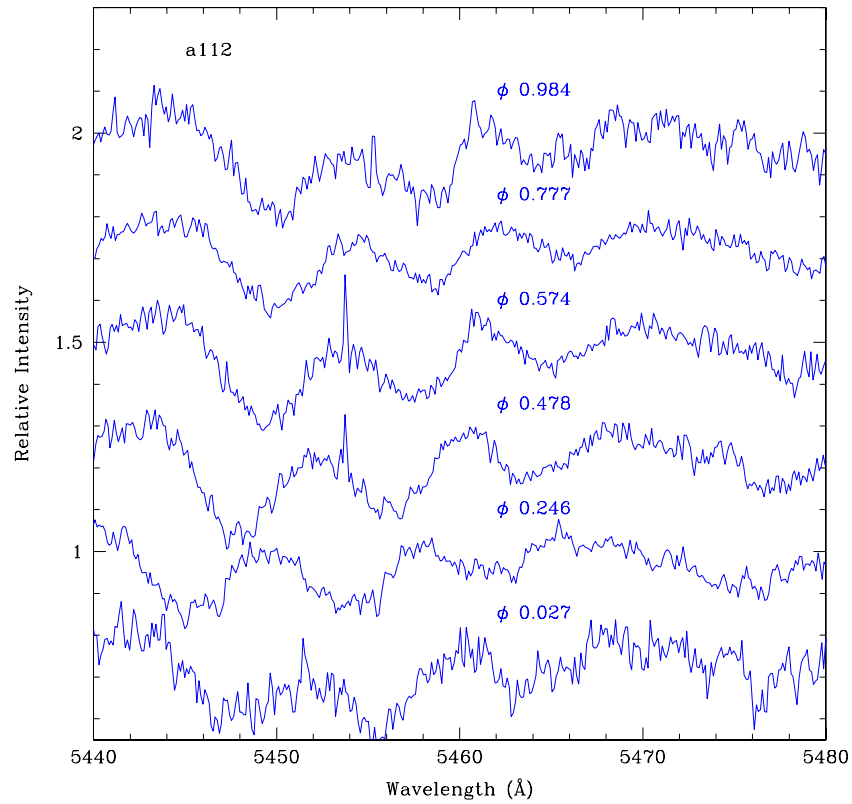
7

Figure 12. Spectra of lines Mg I λ5167, λ5172, λ5183 blend of Fe I lines λ5191.4 through λ5198.7 at various orbital phases (φ). The spectra are from HET HRS order 95 and with the flux normalized to the continuum.

(A color version of this figure is available in the online journal.)

Figure 13. Spectra of lines Fe I λ4957.3, λ4957.6, λ4982.5, λ4983.3, λ4983.8, λ4985.2, λ4985.5, Ti λ4981.7, Na I λ4982.8 at various orbital phases (φ). The spectra are from HET HRS order 95 and with the flux normalized to the continuum.

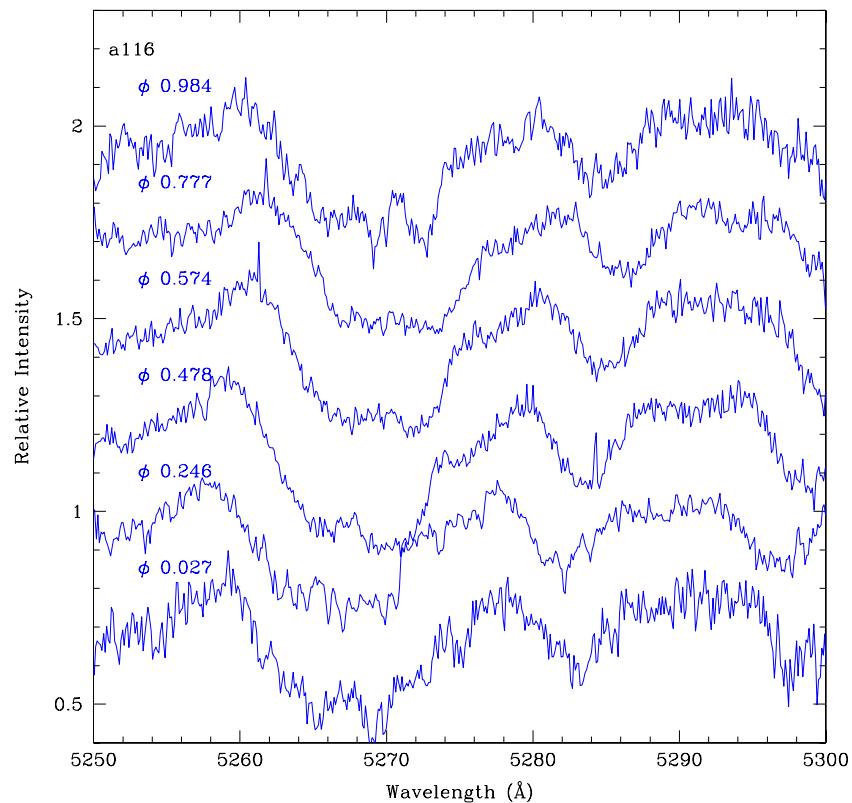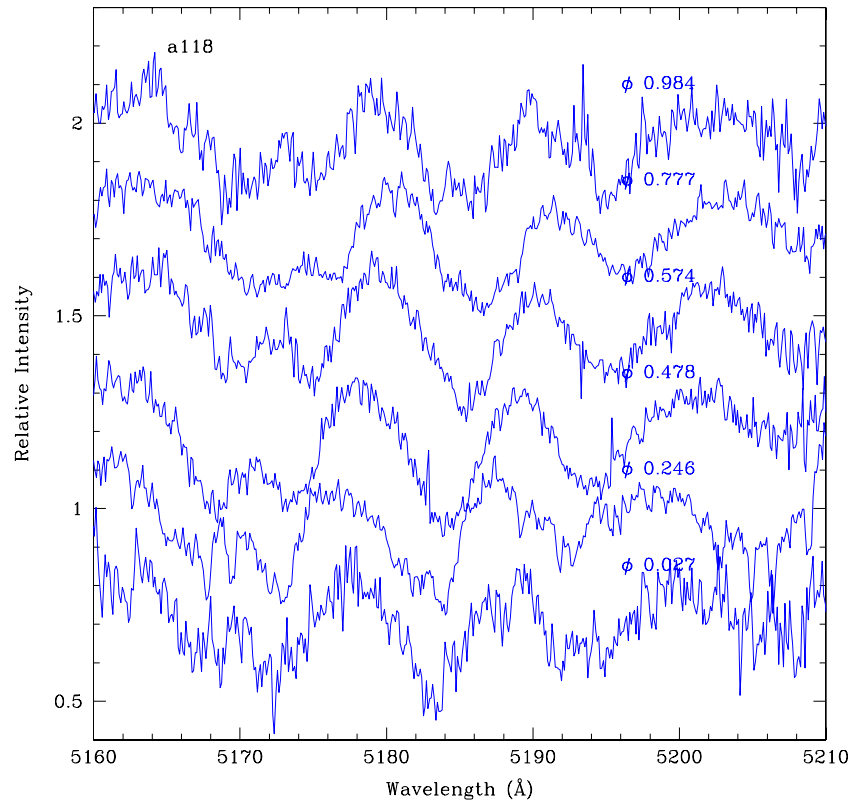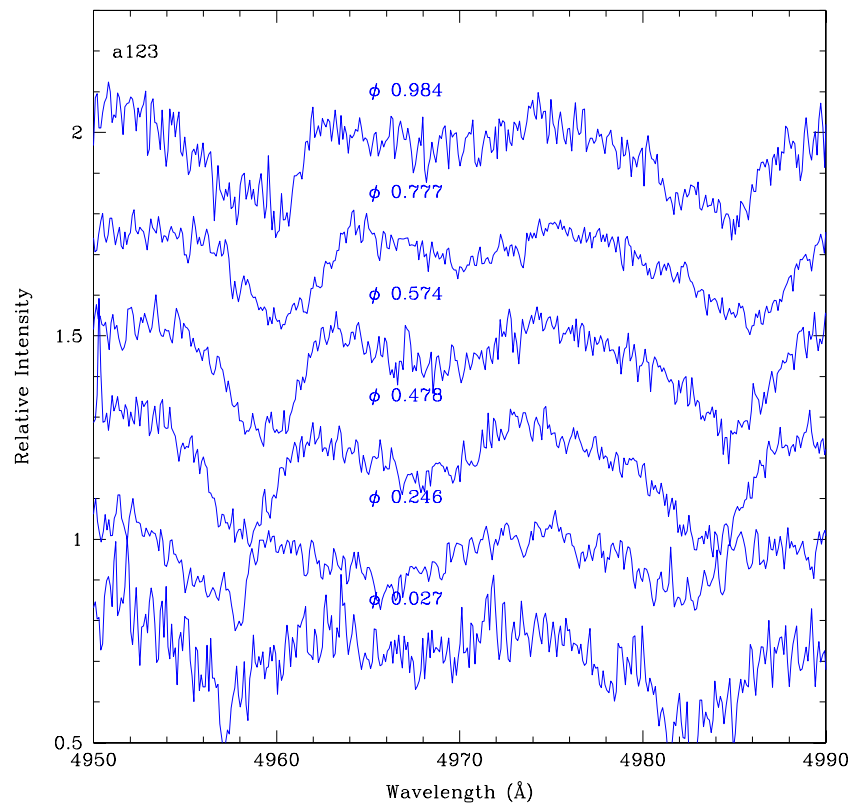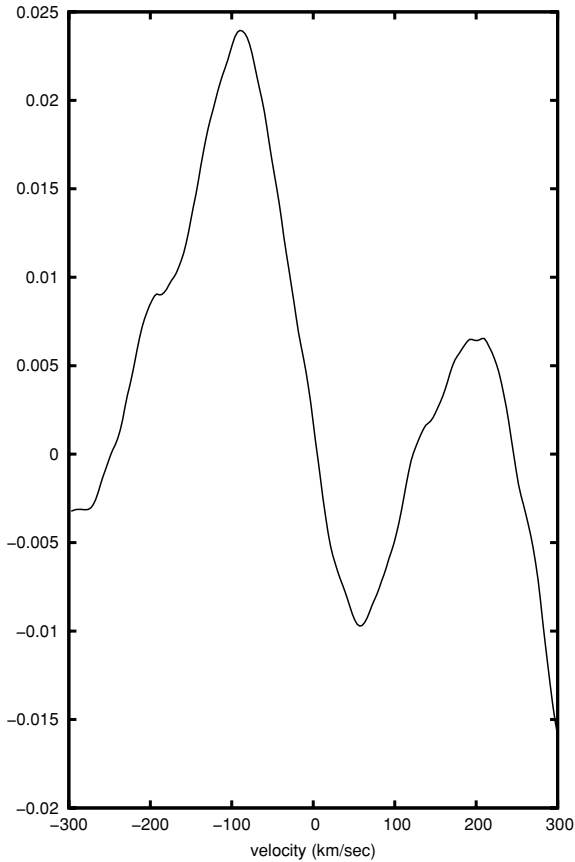(A color version of this figure is available in the online journal.)

Figure 14. Example of the broadening function, in this case for HET order 100 and orbital phase 0.246. The peak on the left is the detection of the primary star velocity and the peak on the right is the detection of the secondary star velocity.

phases where the lines were strongest. To obtain the equivalent widths of just the chromospheric component, we subtracted the photospheric equivalent widths of those lines, which were measured from a K7 spectrum (star 237903) from the Indo-U.S.

Library of Coudé Feed Spectra[9] (Valdes et al. 2004) broadened with a rotational kernel calculated for a vsin(i) value of 135 km s^{-1} (approximate rotational speed of FS Aur-79) and a limb-darkening coefficient of 0.6 (for example, see Gray 2005, p. 465). The error for the measure equivalent widths of the profiles are from the relation given by Cayrel (1988):

$$\Delta EW = \frac{1.6\sqrt{\omega \delta x}}{S/N}, \qquad (1)$$

where ω is the FWHM of the profiles ($\approx$5.5 Å), δx is the pixel size ($\approx$0.1 Å), and S/N is the signal-to-noise ratio in the continuum. The FWHM and S/N were measured using the IRAF task *splot*. The errors of the comparison star spectrum are assumed to be much smaller than the HET spectra. The Hα and Hβ emission lines have the greatest strength at phase 0.0. The emission is weakest near phases 0.25 and 0.75. There is also fairly strong emission near phase 0.5. Our interpretation is that the majority of the chromospheric emission is coming from a region above the secondary and near the neck region. This would cause the greatest amount of chromospheric emission to be visible during phase 0.0, and be more eclipsed by the primary at phase 0.5. Approximately half of the chromospheric emission from that region would then be eclipsed by the secondary and primary at phases 0.25 and 0.75.

Figure 19 shows the ratio of the chromospheric equivalents widths of Hα and Hβ where the error bars are the errors propagated from those shown in Figure 18. The ratio of these equivalent widths ($E_{H\alpha}/E_{H\beta}$) can be used as a diagnostic to determine whether the chromospheric emission is being viewed against the photospheres of the stars ($E_{H\alpha}/E_{H\beta}$ low values) or seen as an extended regions above the limbs of the stars ($E_{H\alpha}/E_{H\beta}$ high values; Hall & Ramsey 1992). Using this diagnostic, we can see from Figure 19 that the chromospheric prominences are being viewed mostly against the photospheres of the stars near phases 0.25 and 0.75, and seen more so above

---

[9] http://www.noao.edu/cflib/
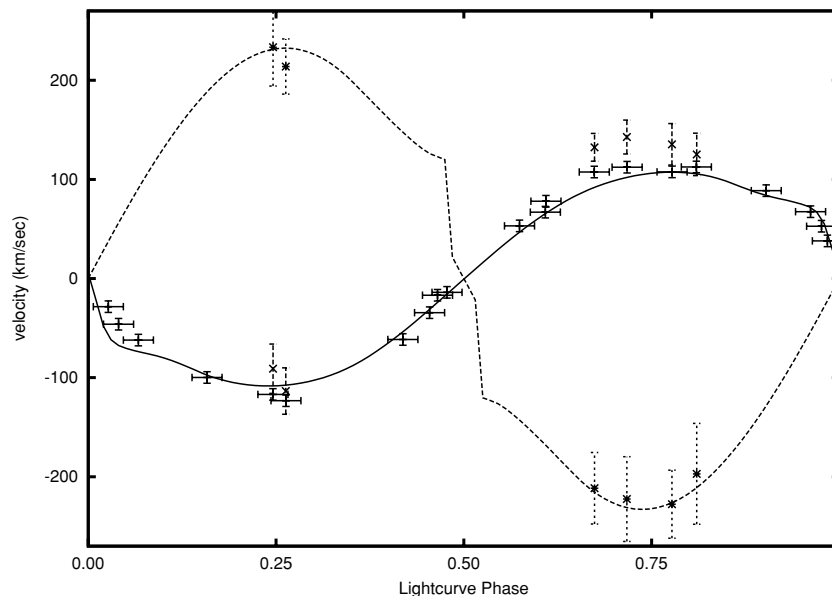
Figure 15. Plusses with *x–y* error bars are the measured radial velocity of the primary from Austin et al. (2007). Crosses with *y* error bars are the radial velocities of the primary determined using spectral broadening functions. Asterisks with *y* error bars are the radial velocities of the secondary determined using spectral broadening functions. The error bars for the broadening function results are the standard deviation over the measured orders. The solid curve is the Wilson–Devinney best-fit model radial velocity curve of the primary star. The dashed curve is the Wilson–Devinney best-fit model radial velocity curve of the secondary star.

Figure 16. Spectra of Hα at various orbital phases (φ). The spectra are from HET HRS order 93 and with the flux normalized to the continuum.

(A color version of this figure is available in the online journal.)

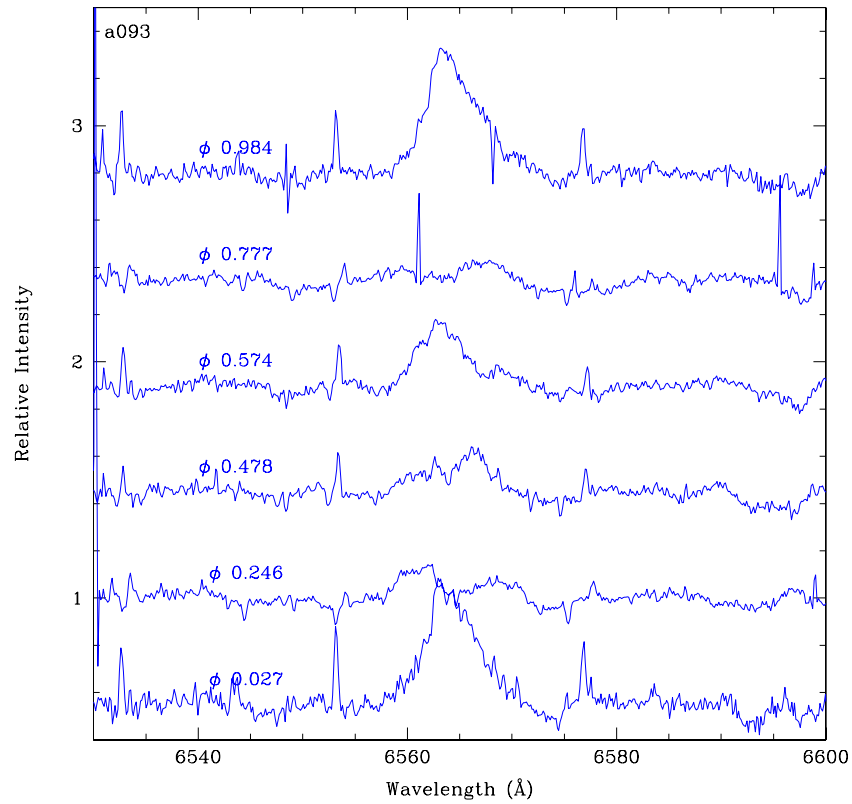**Figure 17.** Spectra of Hβ at various orbital phases (φ). The spectra are from HET HRS order 126 and with the flux normalized to the continuum.

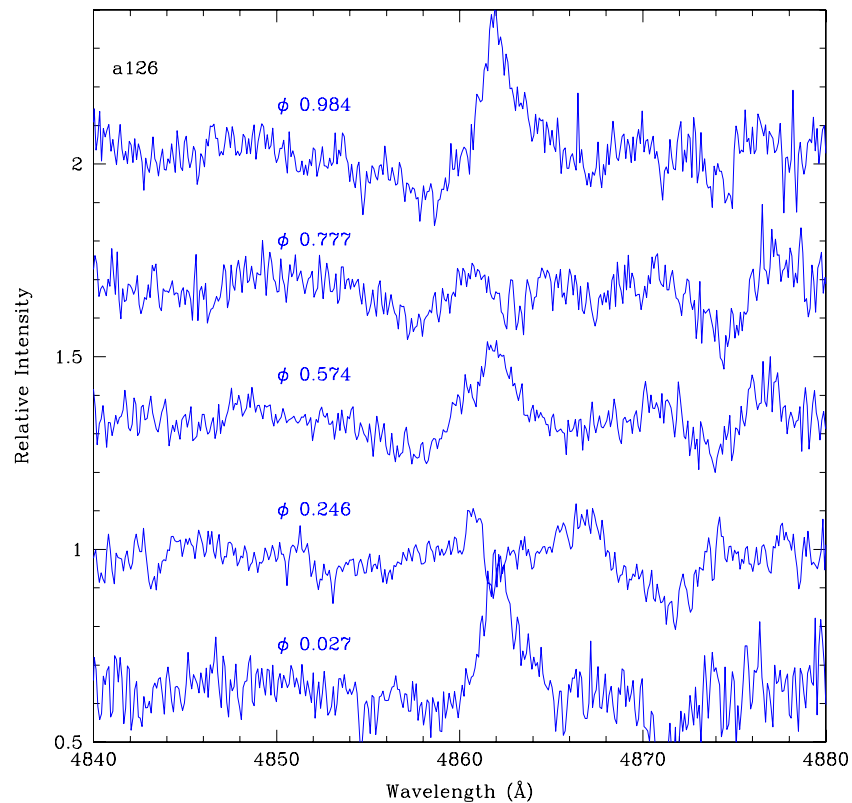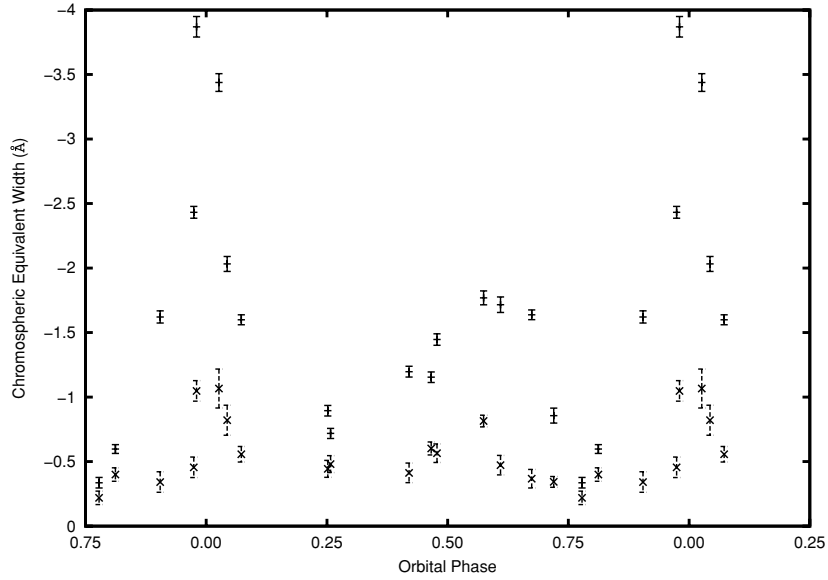(A color version of this figure is available in the online journal.)

Figure 18. Chromospheric equivalent widths of the Hα and Hβ emission lines vs. phase. The plusses with *y* error bars are the equivalent widths of Hα. Crosses with *y* error bars are the equivalent widths of Hβ.
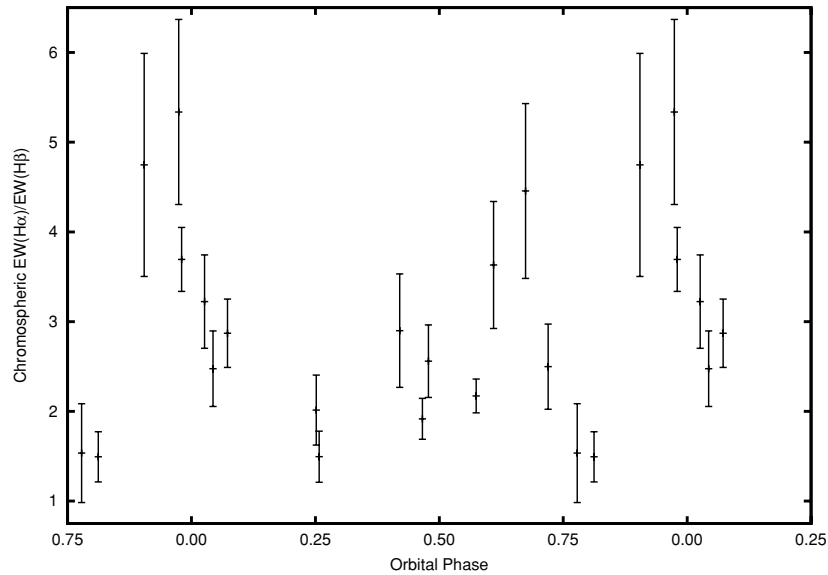

Figure 19. Chromospheric equivalent width ratios of Hα and Hβ emission lines vs. phase.

the limbs of the stars near phases 0.0 and 0.5. This is also consistent with the interpretation that most of the chromospheric prominences are above the secondary and near the neck region.

To further study the location of the chromospheric emission we did DT using the Hα profiles.

3.3. Doppler Tomography of Hα

We have analyzed the Hα emission line from our HET data set using the technique of DT in order to determine in velocity space the location of the sources of emission in the FS Aur-79 system. The geometry of this emission line is provided with the aid of DT techniques (Figure 20). It is particularly important to note that DT (Marsh & Horne 1988) was designed to produce maps of optically thin emission lines of accretion disks of cataclysmic variables. Nevertheless, applications of DT to situations not directly related to its original prescription are abundant in the literature (e.g., Richards et al. 1995; Marsh 2001). To generate the map of Figure 20, we used the maximum

entropy implementation of Spruit (1998), though similar results can be obtained with the application of the filtered back projection reconstruction technique. Nevertheless, the fact that the geometry of FS AUR-79 violates most of the DT axioms (Marsh 2001), it is important to point out that the appearance of spurious artifacts is possible. To address this issue we performed a Monte Carlo simulation on the DT. This procedure works by taking the original data set and producing a large number of different data sets by changing the value of each point in each spectrum according to a Gaussian distribution with mean equal to the true data point and width equal to its flux uncertainty. Subsequently, a different Doppler tomogram is produced for each data set allowing for the construction of a median and a standard deviation map. The uncertainty in each pixel of the Doppler tomogram is then the respective standard deviation of its intensity. In Figure 20, we are only showing regions that have confidence level higher than 1σ, the lighter the region the closer to 1σ it is, where the lightest gray regions are ≈1σ.
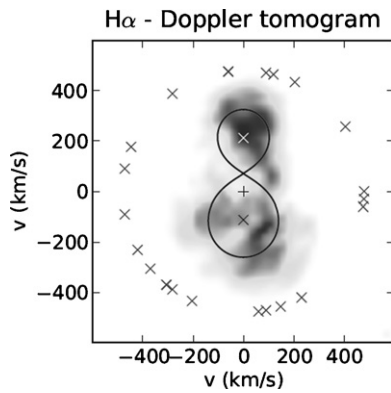
11

Figure 20. Hα Doppler tomogram. Black and white crosses represent the radial velocity positions of the primary and secondary stars, respectively, and the black plus sign represents the velocity of the center of mass. The Roche lobe for a mass ratio of $q = 0.53$ is shown as solid lines, and the crosses represent the directions in which the data were acquired.

The DT of the Hα emission line of FS AUR-79 (Figure 20) places the majority of the emission at the corresponding positions of the primary and secondary star. The emission map is asymmetric and shows a broader profile at the location of the larger and more massive primary star. Interpreting the asymmetries in the tomogram emission profile is not straightforward. Although the majority of the emission arrives from the self-occulting surface of both stars (an effect that is not taken into account by DT), the resulting tomograms are, usually, sensitive to asymmetries on their brightness distribution (Watson & Dhillon 2001). With this in consideration, it is possible to note that the leading region at the primary Roche lobe (regions with $v_x > 0$) shows a considerably higher emission than the opposite region. On the other hand, the emission from the secondary star is more concentrated and stronger than that of the primary star, which may indicate a higher level of activity. In addition, the map also presents evidence of material just outside the Roche lobe of the system, especially around the primary star. The detection of such material may have a significant impact on the magnetic field interaction and braking timescales of both stars (Donati et al. 2000).

The centroids of the emission features on the primary in velocity space in Figure 20 are at longitudes $\approx 117°$ and $\approx 293°$ as measured clockwise from L1. This is generally consistent with the spot configuration on the primary described in Austin et al. (2007) and the modeling described in the next section. One should keep in mind that the Hα emission is due to the chromospheric structure in the system both above and in between the stars, and does not directly map the photospheric spots on the stellar surface (Barnes et al. 2004). But the chromospheric activity is expected to occur near the photospheric spots, but not necessarily at exactly the same position. We cannot give a precise estimate on the position of the emission on the secondary star from the DT because its fractional emission (centered on its center of mass) is greater than the emission from the asymmetric structure.

3.4. Wilson–Devinney Binary Modeling

In Austin et al. (2007), we computed binary star models using Nightfall[10] and Binary Maker (Bradstreet & Steelman 2002) to fit simultaneously the *UBV* photometry and the primary star radial velocity. In this paper, we further check those results by

using the Wilson–Devinney binary star code (Wilson & Devinney 1971) to compute models using the interface and scripting software Phoebe (Prša & Zwitter 2005) as a front end. The full data set fit simultaneously was the *UBV* photometry and primary star radial velocities from Austin et al. (2007), and the secondary star radial velocities determined from the BFs described above (357 data points in all). The model was that of a semi-detached binary, primary star filling its Roche lobe (filling factor = 0), with two circular equatorial star spots on the primary and one circular equatorial star spot on the secondary. Reflection effects were enabled and model atmospheres for the primary and secondary were used. Limb-darkening coefficients were interpolated from the Van Hamme (1993) tables, but given the secondary star temperature the values used were for a temperature of 3500 K. An extensive randomized grid search was carried out covering the parameter space of inclination (i), semi-major axis (a), mass ratio (q), secondary star temperature (T_2), secondary star surface potential (Ω_2), and the spot parameters of longitude, radius, and temperature factor. Given the color and spectrum of the primary star is well established, we held the temperature of the primary (T_1) fixed. Convergence to the final solution was obtained by taking the best-fit solution from the grid search as the starting point for a simulated annealing sequence, forcing it to always step to trial solutions with improved χ^2. Convergence was reached once χ^2 was no longer improved after a few thousand trail solutions. Table 1 lists the parameters and the best-fit values and ranges as well as the resulting masses, radii, filling factors, bolometric magnitudes, and surface gravities. The average radii are listed as are the polar radii, side radii (in the orbital plane perpendicular to the line connecting the centers), back radii (from center to side opposite L_1), and point radii (from center to the same side as L_1).

The reduced chi-squared of the best model found was $\chi^2_{best} = 7.65$. Figures 1–3 show the observed light curves and the best-fit model light curves obtained along with the $O - C$ residuals. Figure 15 shows the measured and computed radial velocity curves for the primary and secondary. The range listed in Table 1 for the semi-major axis is from the uncertainty propagated from the orbital velocity uncertainties. All of the other ranges listed in Table 1 were determined by perturbing each parameter value from its optimal value while holding the other parameters fixed at their optimal values and determining the range where $\Delta\chi^2_\nu \leqslant 1.0$ ($\Delta\chi^2_\nu = \chi^2_\nu - \chi^2_{best}$).

A system inclination of 86°.7 was 3°.4 higher than that found in Austin et al. (2007) but the error bars overlap. The secondary star temperature found of 3455 K was 30 K higher than that found in Austin et al. (2007) and again has overlapping error bars. The primary and secondary star spot longitudes in Table 1 are measured counterclockwise from L_1. Using this convention, the star spots on the primary in Austin et al. (2007) were at 230° and 330°, and here we found to be located at essentially the same positions of $198° \pm 16°$ and $333° \pm 5°$. The secondary star spot is mostly centered on the side facing the primary, much like before. The optimal spot sizes and temperature factors listed in Table 1 are comparable to those found in Austin et al. (2007). Spot size and temperature contrast can be strongly correlated, such that a small cool spot may give the same result as a larger less cool spot, and vice versa over a range of size and temperature. To address this for each spot separately, we mapped the spot-radius–temperature factor space around the optimal values. For each of the two spots on the primary, we found ranges of equivalent models to be confined to mostly dimples in parameter space within the ranges listed in Table 1 for the single parameter

---

[10] http://www.hs.uni-hamburg.de/DE/Ins/Per/Wichmann/Nightfall.html

Table 1
Wilson–Devinney Phoebe Model with Spots

Parameter	Value	Range
Ephemeris		
Period (days)[a]	0.251	
System		
Semi-major axis a ($R_\odot$)	1.66	1.58–1.74
q ($=M_2/M_1$)	0.48	0.47–0.49
i (°)	86.7	84.4–89.5
Components		
T_1 (K)[a]	4100	
T_2 (K)	3455	3435–3478
Surface potential Ω_1 [b]	2.838	2.818–2.857
Surface potential Ω_2	2.891	2.870–2.920
Surface		
Gravity brightening primary and secondary[a]	0.32	
Albedo$_1$ = Albedo$_2$ [a]	0.5	
Limb darkening[c]		
Bolometric linear coefficient X primary	0.59325	
Bolometric linear coefficient X secondary	0.47355	
Bolometric nonlinear coefficient Y primary	0.20416	
Bolometric nonlinear coefficient Y secondary	0.28384	
U linear coefficient X primary	0.793018	
U linear coefficient X secondary	0.836070	
U nonlinear coefficient Y primary	−0.108709	
U nonlinear coefficient Y secondary	0.305191	
B linear coefficient X primary	0.828696	
B linear coefficient X secondary	0.861432	
B nonlinear coefficient Y primary	−0.050568	
B nonlinear coefficient Y secondary	0.331775	
V linear coefficient X primary	0.797432	
V linear coefficient X secondary	0.834432	
V nonlinear coefficient Y primary	0.085901	
V nonlinear coefficient Y secondary	0.324067	
Spot(s) primary (Phoebe coordinates)		
Longitude [1] (°)	198	178–214
Latitude [1] (°)[a]	90	
Radius [1] (°)	71	57–85
Temperature factor [1]	0.994	0.993–0.996
Longitude [2] (°)	333	329–338
Latitude [2] (°)[a]	90	
Radius [2] (°)	74	72–78
Temperature factor[2]	0.977	0.976–0.978
Spot(s) secondary (Phoebe coordinates)		
Longitude [3] (°)	359	350–10
Latitude [3] (°)[a]	90.0	
Radius [3] (°)	54	46–62
Temperature factor [3]	0.869	0.820–0.920
Output		
χ_ν^2	7.65	7.65–8.65
Mass primary ($M_\odot$)	0.667	0.663–0.671
Mass secondary ($M_\odot$)	0.320	0.316–0.325
Average radius primary ($R_\odot$)	0.742	0.737–0.746
Pole radius primary ($R_\odot$)	0.691	0.656–0.722
Side radius primary ($R_\odot$)	0.740	0.702–0.773
Back radius primary ($R_\odot$)	0.790	0.750–0.826
Point radius primary ($R_\odot$)	0.925	0.878–0.967
Average radius secondary ($R_\odot$)	0.508	0.498–0.518
Pole radius secondary ($R_\odot$)	0.478	0.454–0.500
Side radius secondary ($R_\odot$)	0.496	0.471–0.518
Back radius secondary ($R_\odot$)	0.521	0.495–0.545
Point radius secondary ($R_\odot$)	0.622	0.551–0.650
$\Omega(L_1)$ [d]	2.838	2.818–2.857
$\Omega(L_2)$ [d]	2.550	2.535–2.563
Filling factor primary	0.0	
Filling factor secondary	−0.184	−0.111–0.284
M_{bol} primary	6.92	6.91–6.93
M_{bol} secondary	8.49	8.45–8.54
$\log(g)$ primary	4.52	4.51–4.53
$\log(g)$ secondary	4.53	4.52–4.54

Notes.
[a] Held fixed.
[b] Maintained so that the primary star fills its Roche lobe (filling factor = 0).
[c] Interpolated from Van Hamme (1993) tables.
[d] Potential at Lagrange point.

perturbations. Therefore, for the primary spots, the size and temperature of the spots are rather tightly constrained, which means the light curves cannot be reproduced using two small cool spots on that side of the primary, but instead require much of that side of the primary to be cooler than the other side. For the secondary spot, however, there is more of a valley or elongated dimple of equivalent solutions in the spot-radius–temperature factor space, but again, mostly confined within the ranges listed in Table 1 for the single parameter perturbations. Therefore, the size and temperature of the secondary spot region is not as constrained.

4. SUMMARY AND CONCLUSIONS

The radial velocities of the secondary star were found and measured with the BF technique resulting in maximum radial velocities of ≈224 km s⁻¹. The maximum radial velocities predicted from the photometric modeling from Austin et al. (2007) are within the uncertainties of these measurements.

The equivalent widths of just the chromospheric emission of Hα and Hβ show that the chromospheric prominences are the least eclipsed near phases 0.0 and 0.5 and eclipsed the most near 0.25 and 0.75. The equivalent width ratios indicate that the chromospheric prominences are seen mostly against the background of space just before phase 0.0 and again between phases 0.5 and 0.75. These results are reinforced by the DT of Hα. From Figure 20 standing at the phase 0.65 mark, one would see a large amount of emission seen against the background of space that would either be eclipsed or seen against the stellar surface if one were standing at the phase 0.15 mark. Also from Figure 20 standing at phase 0.9 mark one would see a large amount of emission seen against the background of space that would either be eclipsed or seen against the stars if one were standing at the phase 0.4 mark.

The Wilson–Devinney binary star model that best fit the *UBV* photometry and the measured radial velocities has an inclination ≈87°, primary temperature ≈4100 K, secondary temperature ≈3455 K, equatorial spots on the primary at longitudes 198° and 333°, equatorial spot on the secondary at longitude of 359°. The spot locations are in the vicinity of the chromospheric prominences determined from Hα and Hβ equivalent widths. The star spots are photospheric and do not directly map the locations of the chromospheric emission.

Photometry of this system spanning 1999 through 2005 (Robertson et al. 2004; Austin et al. 2007) has yielded a consistent light curve shape showing same asymmetry at quadrature phases (the O'Connell effect) due to the star spots. Therefore, over that time frame it would appear that the longitudes of the spots have been constant. This is consistent with magnetic field modeling of binary late-type stars that predict spotting at preferred longitudes (Moss & Tuominen 1997; Holzwarth & Schüssler 2003a, 2003b). Long-term photometric monitoring of this system could further address the issues of preferred spot longitudes and spot cycles.

Li I λ6708 can be used to constrain the ages of late-type stars given that Li is destroyed over time by the nuclear reactions in these stars. All of our HET HRS spectra include the order for that line. Figure 21 shows the median spectrum from all nights for that order. Li I λ6708 does not appear to be present and its absence can be used to determine a lower limit for the age of the system. Given that the primary star has a temperature of 4100 K and using the results from Hillenbrand et al. (2009) one must conclude that the age of this system has to be at least 500 Myr or older. Therefore, this is not a young system that
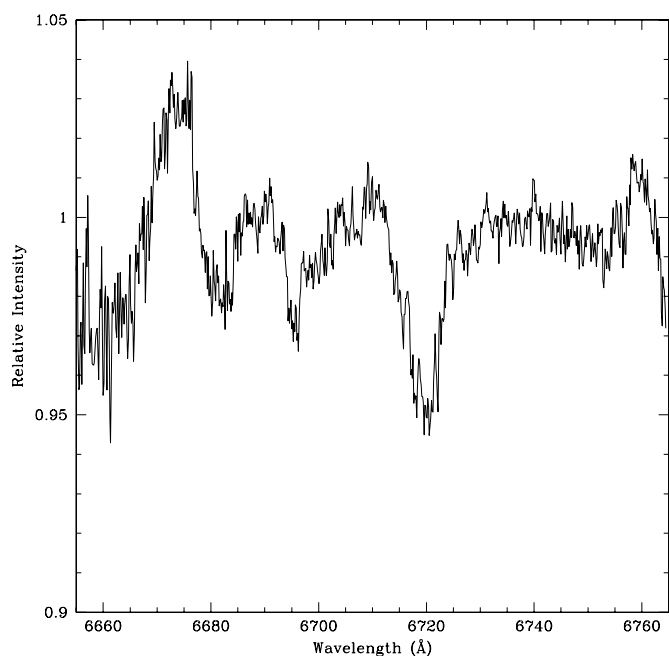
Figure 21. Median spectrum of all phase from HET HRS order 91 and with the flux normalized to the continuum. Ca I λ6717 is present in this spectrum and the age diagnostic line Li I λ6708 is absent.

formed with a close separation, but instead it formed at a much greater separation and has evolved, most likely through angular momentum loss by stellar winds coupled to the magnetic fields, to the current close binary system configuration.

REFERENCES

Austin, S. J., Robertson, J. W., Tycner, C., Campbell, T., & Honeycutt, R. K. 2007, AJ, 133, 1934
Barnes, J. R., Lister, T. A., Hilditch, R. W., & Collier Cameron, A. 2004, MNRAS, 348, 1321
Bradstreet, D. H., & Steelman, D. P. 2002, BAAS, 34, 1224
Cayrel, R. 1988, in IAU Symp. 132, The Impact of Very High S/N Spectroscopy on Stellar Physics, ed. G. Cayrel de Strobel & M. Spite (Dordrecht: Kluwer), 345
Chabrier, G., & Baraffe, I. 1995, ApJ, 451, L29
Donati, J.-F., Mengel, M., Carter, B. D., Marsden, S., Collier Cameron, A., & Wichmann, R. 2000, MNRAS, 316, 699
Gray, D. F. 2005, The Observation and Analysis of Stellar Photospheres (3rd ed.; Cambridge: Cambridge Univ. Press)
Groth, E. J. 1986, AJ, 91, 1244
Hall, J. C., & Ramsey, L. W. 1992, AJ, 104, 1942
Henden, A. A., & Honeycutt, R. K. 1997, PASP, 109, 441
Hilditch, R. W., King, D. J., & McFarlane, T. M. 1988, MNRAS, 231, 341
Hillenbrand, L., Mamajek, E., Stauffer, J., Soderblom, D., Carpenter, J., & Meyer, M. 2009, in AIP Conf. Proc. 1094, Cool Stars, Stellar Systems and the Sun: Proc. of 15th Cambridge Workshop on Cool Stars, Stellar Systems, and the Sun, ed. E. Stempels (Melville, NY: AIP), 800
Holzwarth, V., & Schüssler, M. 2003a, A&A, 405, 291
Holzwarth, V., & Schüssler, M. 2003b, A&A, 405, 303
Hrivnak, B. J., Guinan, E. F., & Lu, W. 1995, ApJ, 455, 300
Hroch, F. 1998, in Proc. 29th Conf. on Variable Star Research, Computer Programs for CCD Photometry, ed. J. Dusek & M. Zejda (Pec pod Snezku, Czech Republic: B.R.N.O.), 30
Jeffries, R. D., Elliott, K. H., Kellett, B. J., & Bromage, G. E. 1993, MNRAS, 265, 81
Maceroni, C., & Montalban, J. 2004, A&A, 426, 577
Marsh, T. R. 2001, Astrotomography, Indirect Imaging Methods in Observational Astronomy, ed. H. M. J. Boffin, D. Steeghs, & J. Cuypers (Lecture Notes in Physics, Vol. 573; Berlin: Springer-Verlag), 1
Marsh, T. R., & Horne, K. 1988, MNRAS, 235, 269
Morales, J. C., et al. 2009, ApJ, 691, 1400
Moss, D., & Tuominen, I. 1997, A&A, 321, 151
Odell, A. P. 1996, MNRAS, 282, 373
Prša, A., & Zwitter, T. 2005, ApJ, 628, 426
Ribas, I. 2003, A&A, 398, 239
Richards, M. T., Albright, G. E., & Bowles, L. M. 1995, Ap&SS, 224, 547
Robertson, J. W., Austin, S. J., Campbell, T., & Hoskins, J. 2004, IBVS, 5536
Rucinski, S. 1999, in ASP Conf. Ser. 185, IAU Colloq. 170, Precise Stellar Radial Velocities, ed. J. B. Hearnshaw & C. D. Scarfe (San Francisco, CA: ASP), 82
Shaw, J. S. 1990, in Active Close Binaries, ed. C. Ibanoglu (Dordrecht: Kluwer), 241
Shaw, J. S., Caillault, J. P., & Schmitt, J. H. M. M. 1996, ApJ, 461, 951
Spruit, H. C. 1998, arXiv:astro-ph/9806141
Stetson, P. B. 1987, PASP, 99, 191
Strassmeier, K. G., Hall, D. S., Zeilik, M., Nelson, E., Eker, Z., & Fekel, F. C. 1988, ApJS, 72, 291
Valdes, F., Gupta, R., Rose, J. A., Singh, H. P., & Bell, D. J. 2004, ApJS, 152, 251
Van Hamme, W. 1993, AJ, 106, 2096
Watson, C. A., & Dhillon, V. S. 2001, MNRAS, 326, 67
Wilson, R. E., & Devinney, E. J. 1971, ApJ, 166, 605